Presented at the 37th European PV Solar Energy Conference and Exhibition, 7-11 September 2020

EFFICIENT DEPLOYMENT OF DEEP NEURAL NETWORKS FOR QUALITY INSPECTION OF SOLAR CELLS USING SMART LABELING

Philipp Kunze[1], Johannes Greulich[1], Stefan Rein[1], Klaus Ramspeck[2],
Marc Hemsendorf[3], Andreas Vetter[3*], Matthias Demant[1]
[1]Fraunhofer Institute for Solar Energy Systems ISE, Heidenhofstr. 2, 79098 Freiburg, Germany
[2]h.a.l.m. elektronik GmbH, Friesstr. 20, 60388 Frankfurt am Main, Germany
[3]GP Inspect GmbH, Hainbuchenring 9-11, 82061 Neuried, Germany
*now with Technical University Munich, Arcisstrasse 21, 80333 München

ABSTRACT: Luminescence images of solar cells show material- and process-related defects in solar cells, which are relevant for monitoring, optimization and processing. Convolutional neural networks (CNNs) allow the reliable segmentation of these defects in images of the solar cells. Nevertheless, the training of CNNs requires a large amount of empirical data, in which the defects have to be labeled expensively by experts. We introduce a method allowing efficient training by using Smart Labels. We show how this technique can be used for process monitoring to detect systematic errors. This approach differs from previous methods, which rely on human heuristics in the form of feature engineering or learning-based methods with human-annotated defects. However, this previous approach has some limitations and risks. These include label mistakes due to overlapping defect structures, poorly reproducible annotations and varying label quality. Furthermore, existing algorithms have to be adapted to new cell lines or a new labeling process is required. We overcome these challenges by avoiding the use of human labels and instead perform the CNN training on the basis of spatially resolved reference measurements, which allows us to calculate spatially resolved labels in less than a second. This purely data-driven approach allows a fast training to quantify defects with physical relevance regarding dark saturation current density (j_0) and series resistance (R_s). The trained CNN achieves a precision of 88% and a recall of 91% for j_0 defects while for R_s defects it attains a precision of 78% and a recall of 86%. The accelerated training process allows a fast deployment of deep learning models in the solar cell line.
Keywords: Solar Cells, Luminescence Imaging, Defects, Defect Detection, Deep Learning

1 INTRODUCTION

Material- and process-related defects, as well as microcracks, can reduce the potential efficiency of a solar cell. The degree of influence depends on the distribution and severity of the defects. Quantifying these properties in luminescence-based measurements is very helpful for both process monitoring and fault analysis. Although there are already several attempts for defect detection, examples are described below, their process of data and label aquisition is often extensive, costly, and potentially error-prone. This paper presents an approach for the efficient generation of physically relevant defect labels and their spatially resolved detection by a deep convolutional neural network (CNN) in inline measurements.

Such defects are visible in several spatially resolved inline and offline measurement images, some of which we use as input or reference images, respectively, and are described in the following. In electroluminescence (EL) measurements [1], both dislocation structures and certain process defects like finger interruptions are visible. In photoluminescence (PL) imaging [2], in contrast, mainly material defects are visible. With the help of a combination of EL and PL measurements, the coupled determination of the dark saturation current and series resistance (C-DCR) imaging, measurement images can be generated which provide a spatially resolved determination of the dark saturation current density (j_0) and the series resistance (R_s) [3]. These two measurement images have been maily used in research and not production, however, Dost et al. show the implementation for inline application [4]. In our approach we use these measurement images to label defects. In other approaches, they are also utilized for the direct training of CNNs [5,6].

There are several attempts that aim at detecting the mentioned defects automatically in inline measurements. They are primarily divided into the categories (i) featured-engineering relying on human-made filters and heuristics and (ii) end-to-end approaches, where the defects are found directly in the measurement images through machine learned filters based on a large dataset. Tsai et al. propose a technique for the detection of microcracks and finger interruptions, where Fourier transformation is used to filter for the defect-related frequencies [7]. In [8] Tseng et al. used the second derivation of the rows of an EL image after a region of interest (ROI) detection to detect finger interruptions. In [9] a new feature descriptor for EL images is presented, which describes the environment of pixels within a gradient based method by a binary code. They use the code for defect detection in form of a clustering approach. Similar feature-engineering approaches for defect identification can be found in [10] and [11]. Regarding end-to-end approaches, a CNN is used in [12] to segment different types of microcracks and finger interruptions in EL images. In [13] Deitsch et al. compare an end-to-end with a feature-engineering approach concerning the detection of defective solar cells in modules. Chen et al. also show the use of CNNs for the inspection of solar cell surface defects visible in photos [14].

All approaches have in common that they are either based on human heuristics or require expert labels, resulting in two problems, which we aim to overcome:

1. Expert labels are poorly reproducible, inconsistent and depend on the experience of the labeling person.
2. The adaptation of labels or heuristics to new cell processes can be very time consuming and expensive.

Problem 1. Expert labels are poorly reproducible, inconsistent and depend on the experience of the labeling person. Alt et al. compared the labels of three trained operators who were supposed to sort 30,000 solar cells into the categories “ok” or ”non-ok” based on EL images. For a total of 4970 cells, at least one operator selected category “non-ok”. But for only about 35% of these cells,

all three operators agreed on this category. They even claim that the label is not always consistent if the measurement is presented repeatedly to the same labeler [15]. Greulich et al. come to a similar conclusion with regard to microcrack labels in luminescence images from six different experts. In a recent study, they show that microcrack labels of six experts vary considerably and none of the experts could find all microcracks in EL images [16].

Problem 2. The adaptation of labels or heuristics to new cell processes can be very time consuming and expensive. It may be necessary to adjust already existing algorithms to other cell processes or to modify them to fit a slight process change or modification of the inspection measurements, which may lead to an enormous effort of renewed labeling. It is not guaranteed that defect detection algorithms will also work for updated cell processes because there might be a different defect distribution and appearance. If algorithms are adapted from multicrystalline silicon (mc-Si) to monocrystalline silicon cells (Cz-Si), or even to quasi-monocrystalline cells, this could lead to a new, costly labeling process.

To address these problems, we propose a new method of label generation that does not have the shortcomings mentioned above, which is denoted as Smart Labeling within this work. The problem of faulty labels can be mitigated by incorporating physical conditions and reference measurements into the labeling process. For dislocation patterns and finger interruptions, spatially resolved offline measurements such as j_0 and R_s images obtained via C-DCR are useful, because the dark saturation current density j_0 at dislocations or the series resistance R_s at finger interruptions is significantly increased. By defining physical threshold values and applying simple image processing techniques, spatially resolved defect labels can be generated quickly and accurately, which are correspondingly less prone to errors and more clearly defined. This automated method of label generation enables transferability to other solar cell designs, which on the one hand, provides flexibility of use and, on the other hand, saves implementation costs otherwise needed for expert labels.

2 APPROACH

The approach consists of three parts: (i) Smart Label Generation, (ii) Smart Label Prediction and (iii) Smart Labels for process monitoring.

2.1 Smart Label Generation

For the Smart Labeling, j_0 and R_s images are calculated from C-DCR measurements, which are used to derive spatially resolved defect labels. Figure 1 shows the process of smart label generation. In the reference measurements, the j_0 image is shown on the left and the R_s image of the same cell on the right. The dark saturation current density is increased at material defects. At finger interruptions, there is a higher series resistance. To calculate the j_0 relevant labels, local variations are first smoothed with a Gaussian filter, so that a continuous transition from high to low j_0 areas is obtained. Subsequently, physical thresholds can be defined within a hysteresis-thresholding procedure, on the basis of which spatially resolved smart labels can be calculated, which are shown in orange. For the R_s relevant smart labels, finger interruptions can be searched by means of applying an anisotropic Gaussian filter perpendicular to the busbar contacts. The resulting labels are shown in green.

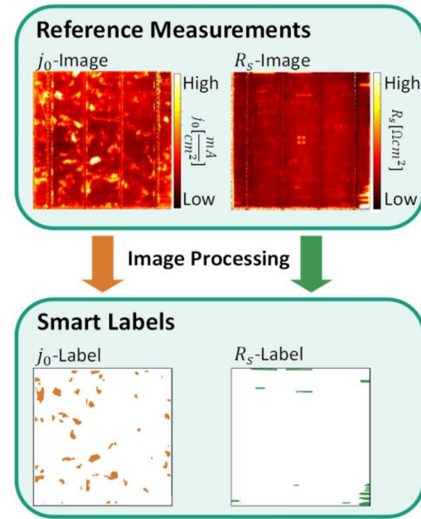

Figure 1: Schematic visualization of the generation of smart labels based on j_0 and R_s images.

2.2 Smart Label Prediction

The objective is to automatically detect labels derived from C-DCR reference measurements in fast inline EL measurements. For this purpose, EL images are used as input. A slightly modified form of the U-Net [17] is choosen to predict the defects. The U-Net has four output channels for which it makes the following classifications per pixel: (i) j_0 defect (ii) no j_0 defect (iii) R_s defect (iv) no R_s defect. The integration of the "no defect" channels (ii) and (iv) was chosen because the two defects can also overlap, e.g., a finger interruption within a dislocation pattern.

2.3 Smart Labels for process monitoring

Smart Labels can be used for process monitoring by superposing the locally resolved j_0 or R_s defects, respectively. During processing, for a certain number of the recently produced cells, the detected defects can be summed up per pixel (1 = defect, 0 = no defect) and divided by the number of samples considered. This results in a value between 0 and 1 for each pixel describing the frequency of a defect at the location. A region with a value close to 1 shows frequent defects, while regions with a value close to 0 have hardly any defects. Regions with high values thus indicate systematic errors that may be process-related, e.g. an R_s defect at the same position all the time can indicate a systematic error in the printing process.

3 EXPERIMENTAL

The experiments performed are shown in Figure 2. There are two columns, Training and Evaluation. Grey areas refer to data and cell numbers, blue areas indicate measurements, orange areas correspond to image processing methods or CNN training and predictions, while green areas indicate evaluations, investigations and applications. The dataset, also described in [18], comprises about 6800 mc-Si and high performance (HP) mc-Si wafers from ten different manufacturers and selected from

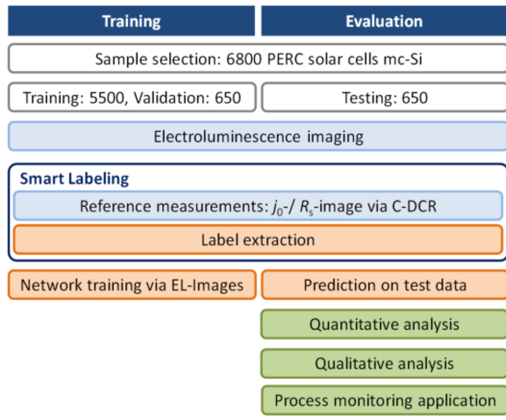

Figure 2: Experimental process.

different bricks at varying brick positions with regular step sizes. The wafers with a size of 156 mm × 156 mm were industrially processed to passivated emitter and rear cells (PERCs). These were randomly divided into three datasets: 5500 (about 80%) were assigned to the training dataset and 650 (about 10%) each to the validation and test dataset.

All cells described were measured using EL- and C-DCR imaging. For the EL measurements, we use a system by h.a.l.m. elektronik GmbH. The cells were excited with 10 A, the integration time of the Si CCD camera was 500 ms and a gain factor of 3 was applied. The following settings were used for the three measurement images required for C-DCR recorded with a system from ISRA Vision AG / GP Inspect with an InGaAs camera under illumination with an NIR laser. The measurements were aligned, meaning cutting off black edges of the measurement images not related to the samples and adjusting the image straight, and were finally available as single channel images with a resolution of $1024 \times 1024\ \text{px}^2$. Based on the procedure described in Section 2.1, Smart Labels were calculated.

A CNN is trained and tested, which receives EL images as input and predicts the defects in a spatially resolved manner. For this purpose, a slightly modified form of the U-Net is used, which has one input and four output channels, as described in Section 2.2. The spatial size of the input and output channels is $256 \times 256\ \text{px}^2$, thus the EL images, as well as the labels, must be scaled to this size. In addition, the EL images are randomly augmented during training using vertical and horizontal flipping, rotation, brightness and contrast changes, and additive Gaussian noise. The Adam Optimizer was used for the optimization with a learning rate of 10^{-3} and a decay of 10^{-5}. Furthermore, the learning rate was reduced by half during training if the validation loss did not reduce within 15 epochs (plateau scheduling). A batch size of 20 was chosen. Based on the validation dataset, the model with the lowest validation loss was selected for further testing.

Three experiments are carried out to show the quality and applications of the trained CNN and Smart Labels:

First, in a quantitative analysis, the spatially resolved prediction is investigated using precision, recall, $F1$-Score, and Intersection over Union (IoU) (see appendix). In addition, the instance detection results are evaluated, meaning whether or not an instance of a defect structure (a defect region disconnected from other defect regions) has been identified. For this purpose, individual separate defect structures with a tolerance of $\pm 20\ px$ are considered as single instances. This means that an instance is considered to be detected correctly if the label pixels match the prediction pixels, whereby a difference of either $20\ px$ too low or too high is tolerated.

Second, within a qualitative investigation, example predictions are used to show which structures are reliably detected and where the prediction deviates from the label.

Third, to test the use of smart labels for process monitoring, the labels of the validation and test dataset are considered. In order to find similar defect distributions, the correlation of each j_0 and R_s label with all other j_0 and R_s labels is calculated. Based on the correlation values, (i) groups of samples with similar defect distributions are identified using K-Means clustering and (ii) the samples are represented as points in a low-dimensional embedding for visualization. Here, two points are placed closer together if they have a high correlation, i.e. a similar defect distribution, and further apart if they have a low correlation, i.e. very different defect distributions. However, the absolute position of the points is not relevant, the visualization serves to compare relatively the defect distributions. The defects are summed up as described in section 2.3 and divided by the number of samples in the respective cluster. In this way, it is investigated at which positions of the cells defects frequently occur.

4 EXPERIMENTAL RESULTS

Quantitative Analysis. Both j_0 and R_s defects can be found by a CNN with high accuracy. Table I shows the prediction results regarding the segmentation, i.e., the pixel-wise classification of both defects. The U-Net finds 91% and 86% of all j_0 and R_s defect pixels, respectively. Especially for the j_0 defects the model is wrong in only a few cases, whereas for the R_s defects a precision of 78% an be achieved. A more detailed description of the quantities used can be found in the appendix.

Table I: Spatially resolved defect prediction results

	Precision	Recall	$F1$-Score	IoU
j_0 defects	0.88	0.91	0.89	0.81
R_s defects	0.78	0.86	0.82	0.70

If closed defect areas are considered as defect instances, it can be evaluated how many of the defect instances are detected regardless of their area. The results are shown in Table II. Due to the tolerance of $20\ px$, a certain inaccuracy might be included in the values. Therefore, they can be considered rather as a tendency. It can be seen that with a recall of 95% many R_s defects can be found. However, since the precision is only 70%, it seems that there are still some instances that are wrongly detected as R_s defects. With a recall of 86% and a precision of 80%, j_0 defect instances are often detected.

Table II: Defect instance detection results

	Precision	Recall	$F1$-Score
j_0 instances	0.80	0.86	0.83
R_s instances	0.70	0.95	0.80

Qualitative Analysis. A qualitative analysis shows that many defects can be reconstructed very accurately and most errors in defect prediction are due to minor deviations from the labels. Figure 3 shows three predictions in (a-c)

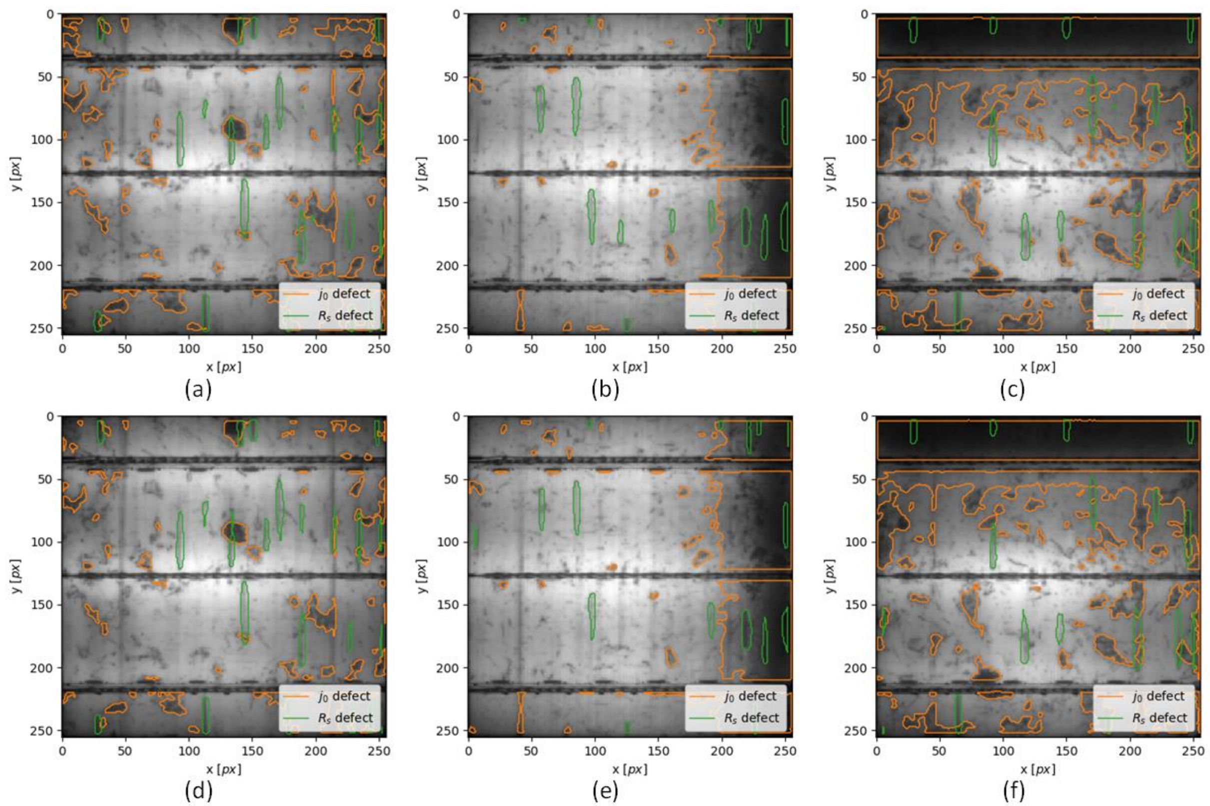

Figure 3: Three predictions with labels for comparison. In (a-c) the predictions of the model are depicted with respect to three EL images. In (d-f) the corresponding smart labels are shown. Orange contours stand for j_0, green ones for R_s defects.

with the corresponding labels in (d-f). Orange contours represent j_0 defects, green contours indicate R_s defects. If the prediction in (a) is compared with the label in (d), they look very similar initially. Small deviations can be seen, for instance, in the upper left corner of the j_0 label or in the size of some finger interruptions. The same can be seen in (b) and (e). Slight inaccuracies occur for the boundary of the dark area at the right margin, which probably results from contamination from the edge of the crucible. Furthermore, the network seems to find too many finger interruptions (centered in the lower half of the cell), which is consistent with the results of the defect instances, shown in Table II. Yet, upon closer examination of the corresponding regions, the prediction is plausible, since the structures are similar to typical finger interruptions and may occur below the thresholds of the smart label generation process.

In the pair in (b) and (e) as well as in the next pair in (c) and (f) it becomes clear that overlapping defect structures can also be distinguished from one another. In the large dark regions on the right and on the top, respectively, which are expressed as a j_0 defect, there are also some finger interruptions located, some of which are hardly visible to the naked eye in the EL image. In both cases, these are reliably detected. Additionally, all examples show overlaps of finger interruptions and dislocation areas within the cell, which are identified independently.

Process Monitoring. Using Smart Labels, process monitoring can be performed with regard to the physically relevant labels. If the defect predictions of sequentially produced cells are superimposed, the frequency of a specific defect can be visualized per pixel. This allows for systematic errors to be detected. The labels of the validation and test dataset were combined to one dataset, so that the analysis can be illustrated for about 1300 cells. Afterward, the correlation of all j_0 and R_s labels to all other j_0 and R_s labels are calculated. As described in section 3, on the basis of the correlation values a low-dimensional embedding for visualization was calculated, we used multidimensional scaling (MDS) [19], and clustering was performed to detect similar defect distributions, for this we used the K-Means-Clustering. In the MDS, points that are close to each other correspond to similar defect distributions and points that are further away from each other have very different defect distributions. Now, the defect frequencies within a cluster can be calculated per pixel.

Some similar defect distributions can be found within the j_0 relevant smart labels. Figure 4 (a) shows on the left side the low-dimensional embedding, where each point represents a cell's j_0 label. The clustering resulted in four clusters, and the points are colored accordingly. To the right of the color bar, the j_0 defect regions within each cluster are superimposed, so that positions, where a defect has occured particularly frequently, are brighter. Since wafers could be rotated during and before processing, similar material defects (represented as j_0 defects) may occur at multiples of 90° rotations of the cell. In order to have rotational invariance for the j_0 defects, all rotations were tested, and the one with the highest correlation was selected for superposition, MDS, and clustering. Cluster 2 seems to have few defects, while the clusters 1 and 4 have regions of reduced lifetime due to contaminations from the crucible at one or two edges, respectively. Cluster 3 shows material defects within the cell. It is noticeable that Cluster 2 is very elongated, which indicates the limited possibilities for the MDS algorithm to represent high-

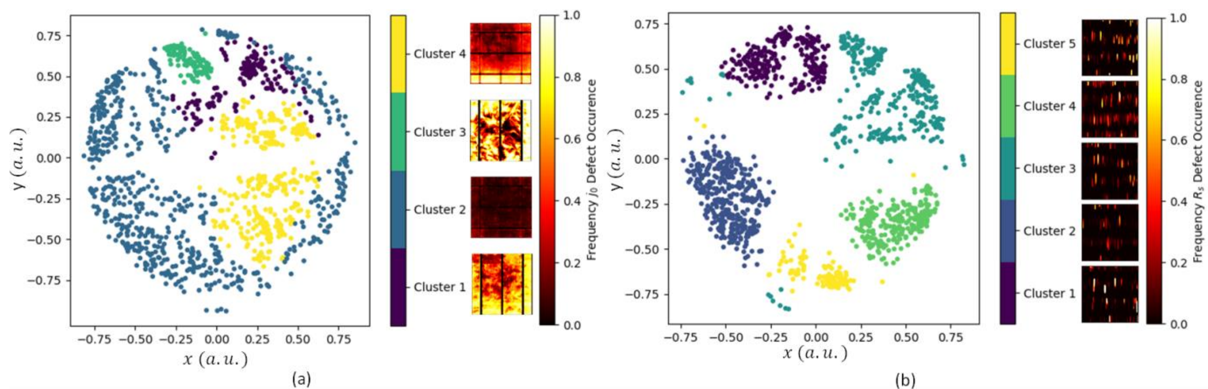

Figure 4: Application of Smart Labels for process monitoring for j_0 defects in (a) and for R_s defects in (b). On the left side of each diagram a low-dimensional embedding based on the correlations of the j_0 (a) and R_s (b) defects is shown, the points are colored according to the clusters found. To the right of the clusters a superposition of the spatially resolved defects per cluster is displayed. Bright areas often show defects at the corresponding locations and accordingly indicate systematic faults.

dimensional data, such as spatial defect distributions, in a low-dimensional way.

A similar result can be seen when considering the smart labels for R_s defects, whose clusters and spatial defect distributions are shown in Figure 4 (b). Five clusters could be identified, and their associated cells always show finger interruptions at certain locations in each cluster. The clusters are well distinguishable from each other both in the low-dimensional embedding and in the defect frequency representations. It is possible that there is a problem within the printing process so that finger interruptions could always occur at similar locations. Some points, especially of cluster 3, could not be positioned correctly by the MDS. However, they show a similar defect distribution as the points of their respective cluster.

5 DISCUSSION

We have shown that physically relevant and spatially resolved, yet binary labels can be generated quickly with the method of smart labeling. The technique can be applied to new cell lines after only minor adjustment to the extraction parameters. Furthermore, they do not depend on the experience and daily condition of the labeling persons. A disadvantage is that the labels are binary labels so that minor defects that fall below the defined thresholds are not labeled as defects. Also, no severity of the defects has been integrated so far. Furthermore, the approach presented is limited to defects related to j_0 and R_s. By integrating further offline references such as the one from Teo et al. to find microcracks [20], the concept can be extended. Another disadvantage is that generally more complex measuring methods, such as C-DCR, are required. However, these would only have to be carried out once in order to train the CNN, so that they could also be executed in external laboratories.

The defects labeled using offline measurements can be learned by CNNs so that they can be detected in inline measurement systems. In EL images, several defects including j_0 and R_s relevant defects are visible. With correct labels, they can be detected with high reliability and speed. This can both extend the characterization of the cells and allow process monitoring. The last predicted smart labels of a cell line can be superimposed, revealing where physically relevant defects occur particularly often. This may be due to process errors. In addition, the correlation of the smart labels can be viewed so that different defect distributions can be identified over a longer period of time, which can also provide information about process and material characteristics. By identifying different defect distribution clusters, it is possible to distinguish e.g. material defect distributions from crucible contaminations, which might be interesting in HP mc-Si and quasi-mono cell processes.

6 CONCLUSION AND OUTLOOK

We presented a method for quantification and spatial segmentation of defects in EL images, which identifies j_0 and R_s relevant defects using a CNN, even if they are overlapping. Our method achieves a recall of 91% and 86% and a precision of 88% and 78% for j_0 and R_s defects, respectively, although the cells are produced by different manufacturers and contain mc-Si and HP mc-Si material. We have shown how prediction can be used for process monitoring, so that systematic and physically relevant defects can be identified.

In this paper, we presented the concept of smart labels, which allows an efficient training of neural networks for defect detection in luminesance images based on spacially resolved meaningful reference measurements. This is achieved because reliable and consistent spatially resolved defect labels can be calculated quickly. Hence, a fast deployment of defect detection networks is possible. In addition, the labels are physically relevant due to the use of reference measurements, which has an advantage over the current labeling process by experts, which is often time-consuming and costly.

In further investigations, we plan to integrate a prediction of the relevance of the individual defects. In addition, we want to show that the technique can be extended to other cell processes and investigate how many reference measurements are necessary for sufficiently accurate detection in inline measurement techniques. Since there are more defect patterns and overlapping structures in mc-Si than in Cz-Si cells, we assume that the method can be applied to Cz-Si cells.

7 ACKNOWLEDGEMENT

This work was funded by the German Federal Ministry for Economic Affairs and Energy within the projects “iMage” (0324045A) and “NextTec” (03EE1001A).

REFERENCES

[1] T. Fuyuki, A. Kitiyanan, Photographic diagnosis of crystalline silicon solar cells utilizing electroluminescence, Appl. Phys. A 96 (2009) 189–196.
[2] T. Trupke, R.A. Bardos, M.C. Schubert, W. Warta, Photoluminescence imaging of silicon wafers, Appl. Phys. Lett. 89 (2006) 44107.
[3] M. Glatthaar, J. Haunschild, M. Kasemann, J. Giesecke, W. Warta, S. Rein, Spatially resolved determination of dark saturation current and series resistance of silicon solar cells, phys. stat. sol. (RRL) 4 (2010) 13–15.
[4] G. Dost, H. Höffler, J.M. Greulich, Advanced Solar Cell Imaging via Luminescence for Industrial Application, to be published (2020).
[5] M. Demant, P. Virtue, A. Kovvali, S.X. Yu, S. Rein, Visualizing Material Quality and Similarity of mc-Si Wafers Learned by Convolutional Regression Networks, IEEE J. Photovoltaics 9 (2019) 1073–1080.
[6] A. Kovvali, M. Demant, T. Trötschler, J. Haunschild, S. Rein, About the relevance of defect features in as-cut multicrystalline silicon wafers on solar cell performance, Lausanne, Switzerland, 2018, p. 130011.
[7] D.-M. Tsai, S.-C. Wu, W.-C. Li, Defect detection of solar cells in electroluminescence images using Fourier image reconstruction, Solar Energy Materials and Solar Cells 99 (2012) 250–262.
[8] D.-C. Tseng, Y.-S. Liu, C.-M. Chou, Automatic Finger Interruption Detection in Electroluminescence Images of Multicrystalline Solar Cells, Mathematical Problems in Engineering 2015 (2015) 1–12.
[9] B. Su, H. Chen, Y. Zhu, W. Liu, K. Liu, Classification of Manufacturing Defects in Multicrystalline Solar Cells With Novel Feature Descriptor, IEEE Trans. Instrum. Meas. 68 (2019) 4675–4688.
[10] S.A. Anwar, M.Z. Abdullah, Micro-crack detection of multicrystalline solar cells featuring shape analysis and support vector machines, in: 2012 IEEE International Conference on Control System, Computing and Engineering, Penang, Malaysia, 2012 - 2012, pp. 143–148.
[11] M. Demant, T. Welschehold, M. Oswald, S. Bartsch, T. Brox, S. Schoenfelder et al., Microcracks in Silicon Wafers I: Inline Detection and Implications of Crack Morphology on Wafer Strength, IEEE J. Photovoltaics 6 (2016) 126–135.
[12] M.R.U. Rahman, H. Chen, Defects Inspection in Polycrystalline Solar Cells Electroluminescence Images Using Deep Learning, IEEE Access 8 (2020) 40547–40558.
[13] S. Deitsch, Automatic Classification of Defective Photovoltaic Module Cells in Electroluminescence Images.
[14] H. Chen, Y. Pang, Q. Hu, K. Liu, Solar cell surface defect inspection based on multispectral convolutional neural network, J Intell Manuf 31 (2020) 453–468.
[15] A. Milan, S. Fischer, S. Schenk, S. Zimmermann, K. Ramspeck, M. Meixner, Electroluminescence imaging and automatic cell classification in mass production of silicon solar cells, IEEE, Piscataway, NJ, 2018.
[16] J.M. Greulich, M. Demant, P. Kunze, G. Dost, K. Ramspeck, A. Vetter et al., Comparison of Inline Crack Detection Systems for Multicrystalline Silicon Solar Cells, IEEE J. Photovoltaics (2020) 1–7.
[17] O. Ronneberger, P. Fischer, T. Brox, U-net: Convolutional networks for biomedical image segmentation, in: International Conference on Medical image computing and computer-assisted intervention, pp. 234–241.
[18] M. Demant, P. Virtue, A. Kovvali, S.X. Yu, S. Rein, Learning Quality Rating of As-Cut mc-Si Wafers via Convolutional Regression Networks, IEEE J. Photovoltaics 9 (2019) 1064–1072.
[19] J.B. Kruskal, Multidimensional scaling by optimizing goodness of fit to a nonmetric hypothesis, Psychometrika 29 (1964) 1–27.
[20] T.W. Teo, Z. Mahdavipour, M.Z. Abdullah, Design of an Imaging System for Characterizing Microcracks in Crystalline Silicon Solar Cells Using Light Transflection, IEEE J. Photovoltaics 9 (2019) 1097–1104.

APPENDIX

The following parameters are used to judge the prediction quality of the model. If a defect is correctly predicted, it is called true positive (TP), if a defect is incorrectly predicted, it is called false positive (FP). If a non-defect is correctly predicted, it is called true negative (TN), if a non-defect is incorrectly predicted, it is called false negative (FN). Some quantities can be derived from this. The precision is defined in equation (1) and indicates how many defect predictions were actually defects.

$$Precision = \frac{TP}{TP + FP} \quad (1)$$

The recall, defined in equation (2), is a measure of how many defects were found of all defects.

$$Recall = \frac{TP}{TP + FN} \quad (2)$$

The F1 score, defined in equation (3), is the harmonic mean of Precision and Recall.

$$F1 - Score = 2\frac{Precision \cdot Recall}{Precsion + Recall} \quad (3)$$

The Intersection over Union (IoU), defined in equation (4), is a measure for spatially resolved predictions and indicates the ratio of the intersection and union of prediction and label. In other words, the IoU is the fraction of correctly predicted defect area.

$$IoU = \frac{TP}{TP + FN + FP} \quad (4)$$